SCIENTIFIC REP♦RTS

OPEN

# Fingerprint of local disorder in long range ordered isometric pyrochlores

Laura Martel, Mohamed Naji, Karin Popa, Jean-François Vigier & Joseph Somers

The detailed characterization of local order and disorder in isometric $A_2B_2O_7$ crystalline pyrochlores is of significant importance in view of their wide range and sensitive technological applications. Nevertheless, much remains to be understood concerning their atomic scale structures. Here we specifically pinpoint local order and disorder in four stoichiometric $Ln_2Zr_2O_7$ (Ln = La, Nd, Sm and Eu) pyrochlores using a combination of three standard easily available laboratory techniques: XRD, ^{17}O solid-state MAS NMR and Raman spectroscopy. The evolution of the oxygen sub-lattice identifies specific features (extra ^{17}O NMR signals and Raman bands) which undoubtedly reveal local oxygen order and disorder in these stoichiometric long range ordered crystalline pyrochlores. These results complete the understanding of the atomic scale in these stoichiometric pyrochlores necessitating the need for new microscopic structural models.

Crystalline $A_2B_2O_7$ pyrochlores have been extensively studied as matrices for immobilization of nuclear waste[1–7] and have a wide range of chemical applications (for e.g.: Li-ion battery[8,9], photoluminescence[10,11], laser materials[12], solid oxide fuel cells[13,14]…). They possess exotic physical properties[15–18] exuding a strong interest in their modelling and simulation[19,20]. Part of their diversity lies in their high sensitivity to order and disorder which is often associated with the crystalline transition between ordered pyrochlore and the disordered fluorite structures[21–25]. Disorder can experimentally be due to oxygen non-stoichiometry[26], cation substitution (e.g. solid-solution)[27], or more extreme conditions such as irradiation[2,4] temperature or pressure[28]. The order-to-disorder process in pyrochlores is described in the literature as being governed by the energetics of defect formation determined by the ratio of the cation ionic radii RR = RR = $r_{A^{3+}}/r_{B^{4+}}$ 1.46 to 1.80[29]. More recently, by using powerful atomistic computer simulation methods[19,30], it has been defined that a disorder enthalpy above ~2.6eV was an efficient way to identify an ordered pyrochlore structure. In an ordered pyrochlore (see Supplementary Figure 1), there are two different crystallographic oxygen sites, a (O2, 48f) site coordinated by two A and B cations and a (O1, 8b) site surrounded by four A cations. One must also consider the ordered oxygen vacancies (V_O, 8a) surrounded by four B cations, which are located in the second coordination sphere of the (O2, 48f) sites. In the defective fluorite structure, there is a complete mixing of the cation sites and the 8a site becomes fully occupied by (O3, 8a) oxygen atoms. This leads to a crystallographic structure where there is no more distinction between the (O1, 8b), (O2, 48f) and (O3, 8a) sites and with an occupancy of 56/64 = 7/8 for each site. In between the ordered pyrochlore and the disordered fluorite, some disordered pyrochlores have been described[31,32].

Our attention has been triggered by the lanthanide zirconate series, and more specifically $La_2Zr_2O_7$ (RR = 1.61), $Nd_2Zr_2O_7$ (RR = 1.54), $Sm_2Zr_2O_7$ (RR = 1.5) and $Eu_2Zr_2O_7$ (RR = 1.48) which on the basis of defect formation energies[29] and disorder enthalpies (i.e. above ~2.6 eV)[19,30] should all be fully ordered pyrochlores. It is worth mentioning that compared to other pyrochlore families, this series nevertheless possess a higher tendency to disordering[19,33]. Interestingly, a literature screening for formally the same stoichiometric $Ln_2Zr_2O_7$, shows numerous values of the lattice parameters (See Supplementary Figure 2), which is often taken as the main parameter to characterize these materials. Indeed, some parameters as the stoichiometry[26,34] or synthesis conditions can influence its value, but, this observation clearly questioned the current experimental characterization of their local structures. A technique such as neutron total scattering has recently been very efficient to investigate the local order allowing the identification of domains with the Weberite structure at the local scale within a defected

European Commission, DG Joint Research Centre-JRC, Directorate G - Nuclear Safety and Security, Postfach 2340, D-76125, Karlsruhe, Germany. Correspondence and requests for materials should be addressed to L.M. (email: laura.martel@ec.europa.eu).

1
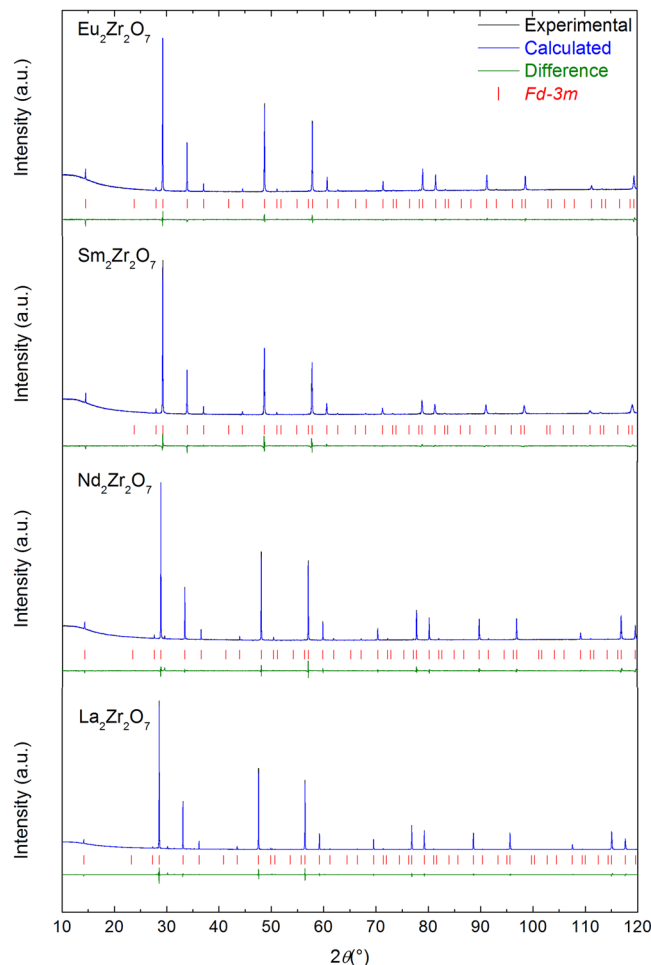
Figure 1. XRD patterns of the $Ln_2Zr_2O_7$ pyrochlore and their corresponding Rietvield refinement depicting the high crystallinity of the $Ln_2Zr_2O_7$ samples.

fluorite structure at the large scale[27]. Unfortunately, due to their high neutron absorption cross sections, this technique cannot be applied to the $Ln_2Zr_2O_7$ with Ln = Sm, Eu and Gd[35]. Though other techniques have been used to probe the local order and disorder in this $Ln_2Zr_2O_7$ pyrochlore series at different length scales, they have suffered by virtue of their indirect approach and disorder was unveiled by detecting an anomaly in the trend of the resulting parameters over the full series of pyrochlores. Thus, Zr-XANES yields a variation of the Zr-coordination number[35] and Raman spectroscopy a broadening of the bands[31]. In the present communication, the structural complexity has been unravelled by XRD, to probe the long range order, and ^{17}O MAS NMR and Raman spectroscopy to elucidate changes in the oxygen local environment of these four stoichiometric rare earth pyrochlores. Thereby, it was possible to detect directly this important subtle order-to-disorder variation by probing the local O-atom environment. The observations reported here are of acute importance as they form the basis for the complete understanding of what is essentially "an ordered pyrochlore structure".

Results

The XRD patterns of the four well crystallized pyrochlores are presented in Fig. 1 confirming their purity (a small non-characterized impurity was identified in the pattern of $La_2Zr_2O_7$). The patterns possess the characteristic superstructure peaks of cubic pyrochlore, Fd-3m and the lattice parameters of 10.8019(1), 10.6911(1), 10.5753(1) and 10.5533(1) Å were obtained for respectively $La_2Zr_2O_7$, $Nd_2Zr_2O_7$, $Sm_2Zr_2O_7$ and $Eu_2Zr_2O_7$. These values are in general agreement with the one previously published[26,34,36–44] and, especially with stoichiometric pyrochlores. As expected, there is an increase of the lattice parameter as a function of the ionic radii (Supplementary Figure 2). As both ^{17}O MAS NMR and Raman spectra present similarities for $La_2Zr_2O_7$ and $Nd_2Zr_2O_7$, we will describe them together. Their ^{17}O MAS NMR spectra depicted in Fig. 2 both possess two ^{17}O signals at 623.3 (A) and 388.7 (B) ppm for $La_2Zr_2O_7$ and at 3890 (C) and 434 (D) ppm for $Nd_2Zr_2O_7$. In addition, an important set of spinning sidebands due to first order quadrupolar interaction (see Supplementary Figure 3) for peak B ($C_Q = 121$ kHz, $\eta_Q = 0.7$) and D ($C_Q = 635$ kHz, $\eta_Q = 0.8$) are detected. This characteristic pattern of spinning sidebands is linked to local distortions around the O site as described elsewhere[45,46]. Therefore Peaks B and D can be both attributed to the (O2, 48f) site and consequently, peaks A and C to the (O1, 8b) site. For $La_2Zr_2O_7$, this attribution is confirmed by the relative intensity between peaks B and A which is 6:1 as expected from its crystal structure. Even
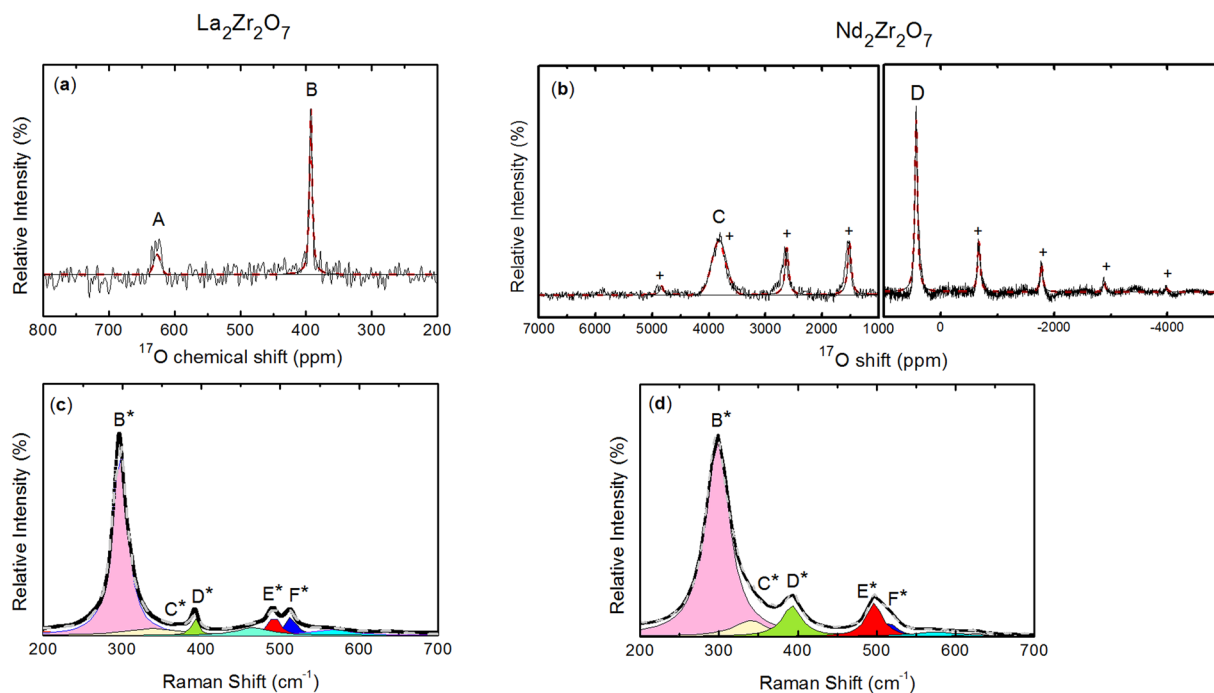
Figure 2. ^{17}O MAS NMR spectra (black) and their corresponding fits (dashed red) acquired at 60 kHz for (**a**) La$_2$Zr$_2$O$_7$ and (**b**) Nd$_2$Zr$_2$O$_7$ (the crosses show the spinning sidebands). And, the Raman spectra (black) of (**c**) La$_2$Zr$_2$O$_7$ and (**d**) Nd$_2$Zr$_2$O$_7$ and their corresponding fits.

if the ^{17}O MAS NMR spectrum of Nd$_2$Zr$_2$O$_7$ is only qualitative (as it was acquired using two offsets), the large ^{17}O NMR shift of peak C conforms with O atoms surrounded by four Nd^{3+} spin bearing centres with unpaired electrons (see Supplementary Note 1)[47–50]. The Raman spectra of La$_2$Zr$_2$O$_7$ and Nd$_2$Zr$_2$O$_7$ can both be reproduced by a set of five Lorentzian bands corresponding to the most obvious vibrational modes[28]. They are labelled B*, C*, D*, E* and F* with Raman frequencies at 297, 339, 392, 492 and 513 cm^{-1} for La$_2$Zr$_2$O$_7$ and 298, 339, 392, 497, 515 cm^{-1} for Nd$_2$Zr$_2$O$_7$, respectively. Two extra weak Raman bands at about 464 cm^{-1} and 561 cm^{-1} were necessary to reproduce the shape of the E* and F* doublet in La$_2$Zr$_2$O$_7$ and are very likely due to the impurities detected by both XRD and ^{17}O MAS NMR as they were not detected in reference[28].

Interestingly, both ^{17}O MAS NMR and Raman spectra of Sm$_2$Zr$_2$O$_7$ and Eu$_2$Zr$_2$O$_7$ presented in Fig. 3 differ strongly from the La and Nd pyrochlores. The ^{17}O MAS NMR spectrum of Sm$_2$Zr$_2$O$_7$ possesses four peaks at 306.2 (E), 249.3 (F), 210.8 (G) and −60.3 (H) ppm with relative intensities of 13, 61, 12 and 14%. Due to its ^{17}O NMR shift, peak H can be attributed to oxygen atoms in the (O1, 8b) site (See Supplementary note 1) while peak F can only be attributed to (O2, 48f) due to its high relative intensity and important spinning sideband pattern. Taking the most obvious features in the Eu$_2$Zr$_2$O$_7$ spectrum, three main peaks can be identified at −196 (I), −767.5 (J) and −3033.3 (K) ppm. This sample exhibits important spectral broadening due in part to the paramagnetic effect as observed in other Eu-based materials[51–53]. Considering its ^{17}O NMR shift, peak K can be attributed to O atoms at the (O1, 8b) site (See Supplementary note 1). Even if the current spectrum is qualitative, peaks I and J are derived from local disorder with one of them emanating from the (O2, 48f) sites. For both samples, spinning sidebands are detected for all the peaks: peak E (C_Q = 1412 kHz, η_Q = 0.7), peak F (C_Q = 756 kHz, η_Q = 0.5), peak G (C_Q = 1067 kHz, η_Q = 0.6), peak H(C_Q = 1067 kHz, η_Q = 0.6), peak I (C_Q = 874 kHz, η_Q = 1), peak J (C_Q = 1237.57 kHz, η_Q = 1) and peak K (C_Q = 528 kHz, η_Q = 0.8).

The Raman spectrum of Sm$_2$Zr$_2$O$_7$ seems very similar to that of the La and Nd counterparts, but, an additional band must be introduced at 191 cm^{-1} (A*) to reproduce the low frequency tail of the spectrum. The remaining five bands at 296, 336, 392, 523 and 588 cm^{-1} are designated as B*, C*, D*, G* and H*. For Eu$_2$Zr$_2$O$_7$, six bands at 198, 296, 332, 390, 533 and 594 cm^{-1} attributed to A*, B*, C*, D*, G* and H* were also identified, albeit with a substantial increase of the line broadening. The fitted Raman band parameters have been plotted in Fig. 4.

Discussion

The main finding of this research is the specific identification of local disorder in each of these pyrochlores, whose derivation presented in Supplementary note 2 has been achieved on collective examination of the entire series, as commonly done. We can now start our discussion with ^{17}O MAS NMR as it is a proven powerful tool to probe local order and disorder in crystalline pyrochlore[54]. The fully ordered stoichiometric pyrochlore structure possesses only two distinct crystallographic O sites; the presence of more than two O signals on the ^{17}O MAS NMR spectrum immediately signifies a local disorder at the atomic scale. This is clearly observed for Sm$_2$Zr$_2$O$_7$ and Eu$_2$Zr$_2$O$_7$ for which no impurities were detected by XRD. As the ^{17}O MAS NMR spectrum of Sm$_2$Zr$_2$O$_7$ was acquired under quantitative conditions we give it more attention. The intensity ratio of peaks (E, F, and G): peak
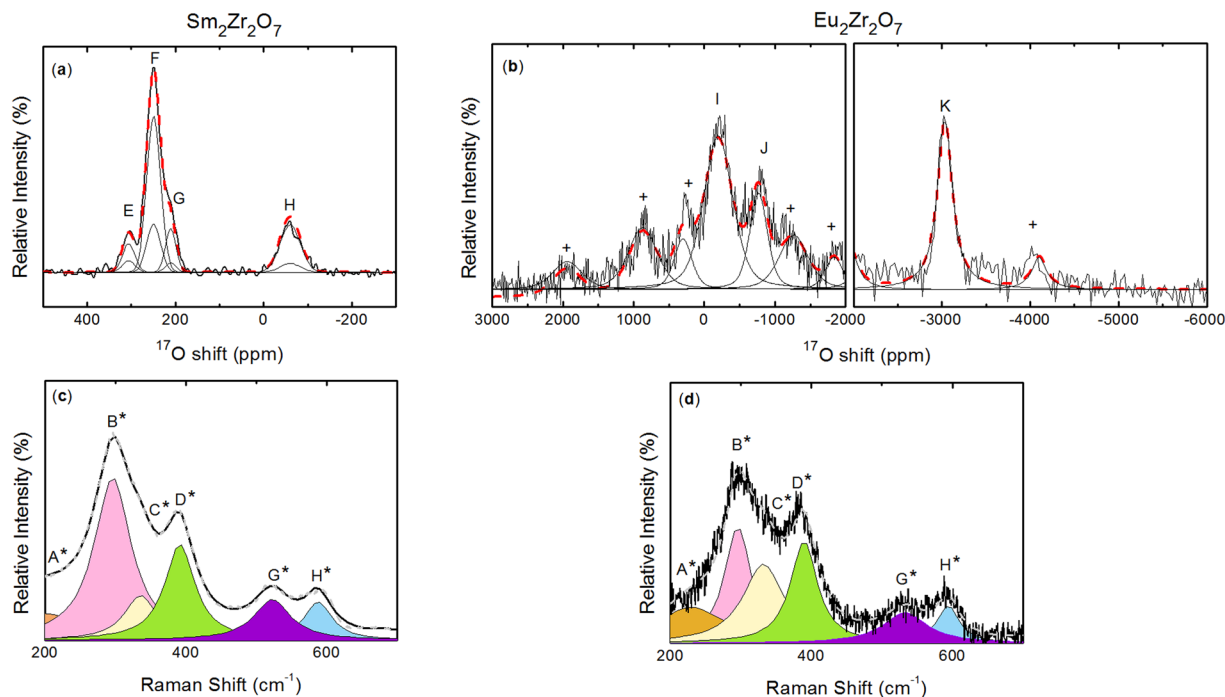
Figure 3. ^{17}O MAS NMR spectra (black) and their corresponding fits (dashed red) of (**a**) $Sm_2Zr_2O_7$ and (**b**) $Eu_2Zr_2O_7$ acquired at 60 kHz (the crosses show the spinning sidebands). And, the Raman spectra (black) of (**c**) $Sm_2Zr_2O_7$ and (**d**) $Eu_2Zr_2O_7$ with their corresponding fits.
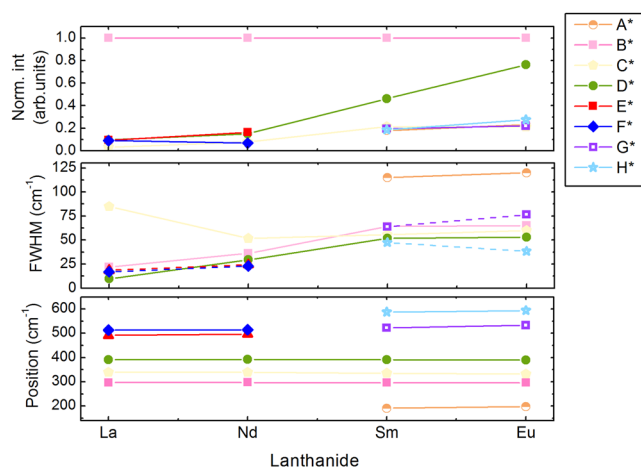
Figure 4. Variation of Raman parameters – band position, FWHM and normalized intensity- as a function of the lanthanide cation. Solid lines serve as guides for the eye. The slightly higher FWHM for band C* in $La_2Zr_2O_7$ might be due to to the overlapping between this band and the one of an impurity.

H is 6:1, i.e. exactly the ratio expected between the two different crystallographic sites (O1, 8b) and (O2, 48f). The intensities of peak E, G and H are very similar, but cannot be simply ascribed to a depopulation of the (O2, 48f) sites into the vacant (V_O, 8a) sites, as this would imply full occupancy of the vacancies. Therefore, the mechanism underlying the disordering seems to be more complex than expected for a simple depopulation of the (O2, 48f) sites. This NMR observation could have been due to the presence of a cationic disorder in our samples, but, the fitting of the XRD patterns considering this type of disorder did not improve the Rietveld refinement (not shown). The increase of disorder is also seen when comparing the ^{17}O MAS NMR spectra of the two ordered pyrochlores with those of the two disordered pyrochlores, one can notice the apparition of spinning sidebands for peak H and K (contrary to peaks A and C) which correspond to the oxygen at the (O1, 8b) sites. This reveals an increase of the local distortion around the O atoms (See Supplementary note 3)[55]. As the cation size decreases through the series, a steric effect cannot be at the origin of these bond distortions, but in contrast, it can be linked to an

increasing disorder in the second coordination shell. A first glance of answer can nevertheless be given to understand this anionic disorder based on the previous Zr-XANES results which showed a change of coordination number through the $Ln_2Zr_2O_7$ series associated to a growing disorder through the series[35].

Accordingly, the second and most convincing proof is found in the Raman vibrational mode assignment, a key pointer in the understanding of the competition between order and disorder. Alarmingly, many discrepancies exist in published assignments thereof[56–58]. The most common method to interpret the Raman data relies on the spectral comparison with each other and between different pyrochlore families[42–44]. Here, we take an alternative approach and attribute the different modes by comparing the spectra through this $Ln_2Zr_2O_7$ series. The five characteristic Raman bands detected for the ordered $La_2Zr_2O_7$ and $Nd_2Zr_2O_7$ have similar frequencies as those previously published supporting the presence of local order and their good stoichiometry[28,59]. Importantly, the energy of all modes seems to be independent of the lanthanide cation except for the E* mode for which a clear upshift is observed when substituting La with Nd (see Fig. 4 and Supplementary Figure 4). This is in good agreement with the atomic displacement analysis[58] for these modes and supports their attribution to pure oxygen motions, except for the E* mode where a small contribution from Ln^{3+} might be present. Armed with a characterization of the Raman spectrum of these two ordered pyrochlores, we analysed those of the disordered pyrochlores. We want to stress that as the main topic of this paper is to show the presence of local disorder at the atomic scale, we did not attempt a full characterization of the Raman modes. We therefore focus our discussion on modes A*, E*, F*, G* and H* which differ between ordered and disordered pyrochlore spectra. As mode A* appears in the spectrum of $Sm_2Zr_2O_7$ and $Eu_2Zr_2O_7$ (its absence is also confirmed in their equivalent ^{16}O Raman spectra reported in literature[28,43,44]) it is unlikely that neither involves (O1, 8b) nor (O2, 48f) oxygens, since both sites are fully occupied in the ideal pyrochlore. To better understand the mode A*, we have to pursue our discussion of the other Raman bands. Our main observation is that G* and H* modes correspond to E* and F* modes, but shifted to higher Raman frequencies. Though, the shift from E* to G* can be explained by the decrease of the lanthanide ionic radii (or increase of the force-constant) the $70\,cm^{-1}$ upshift of F* to H* is unlikely to be caused by the same effect. When considering the Raman data for $La_2Zr_2O_7$ to $Nd_2Zr_2O_7$, there is the previously discussed upshift of mode E* to slightly higher frequency which continues for $Sm_2Zr_2O_7$ (Supplementary Figure 4). But, in the case of mode F*, there is no variation of the Raman band energy from $La_2Zr_2O_7$ to $Nd_2Zr_2O_7$ which should, according to the same logic, lead to an upshift of mode F* of at least $10\,cm^{-1}$. To support this statement, we took account of the previously published force constant change which confirms that the predicted splitting should not exceed 10 to $20\,cm^{-1}$[60]. The difference in frequencies observed here between F* and H* is therefore far too high. Finally, ab initio calculations also seem to predict a mode at $617\,cm^{-1}$ but, unfortunately, for the optically inactive F_{1g} symmetry instead of the F_{2g} symmetry expected for mode F*[61]. Based on all these evidences, we can safely propose that the two well resolved modes E* and F* in $Nd_2Zr_2O_7$ and $La_2Zr_2O_7$ actually merge to form the broad band G* for $Sm_2Zr_2O_7$ and this "merging" is caused by the apparition of the anionic disorder. While mode G* belongs to the ideal pyrochlore structure, it is definitely not the case for mode H* whose observation might be a result of symmetry breaking due to an inherent disorder in the O sites. Therefore, this band is derived from the Zr-O stretching motion modified due to interstitials in the Zr-environment. With this in mind, we can come back on the low frequency mode A* which can be attributed to the vibration of oxygen atoms at the centre of Zr_4O tetrahedral due to interstitial O atoms.

The important redefinition of both these additional vibrational Raman bands inaccurately assigned in the literature, in addition to the ^{17}O MAS NMR analysis, specifically describe the inherent O local order in stoichiometric $La_2Zr_2O_7$ and $Nd_2Zr_2O_7$ and disorder in stoichiometric $Sm_2Zr_2O_7$ and $Eu_2Zr_2O_7$. It is worth mentioning that considering the previously calculated disorder enthalpy formation (both cationic and anionic)[19,30], both $Sm_2Zr_2O_7$ and $Eu_2Zr_2O_7$ belong to the same range of defect energy formation. Even more interesting for this same family, the Raman spectrum[31] of $Gd_2Zr_2O_7$, which also belongs to this range of energy, possesses the specific bands that we presently clarified through the text and characteristic of disordered pyrochlore. These observations might underline the range of energy delimiting ordered from disordered stoichiometric pyrochlore. Finally, our present study can easily be extended to any pyrochlore system but also, implemented to solid-solution or to their modelisation using computational methods. We can safely state that it will help assisting in the construction of a complete understanding of these complex and of high technological importance systems.

Methods

Synthesis. Polycrystalline samples of $La_2Zr_2O_7$, $Nd_2Zr_2O_7$, $Sm_2Zr_2O_7$, and $Eu_2Zr_2O_7$ were produced by liquid route. For this purpose, exceptionally accurate devices for weight (analytical balances of 5 decimals) and volume (fix volume pipets) measurements have been used. Thus, the possible deviations from the stoichiometry were controlled during all the production flux. Solutions of Ln^{3+} (La^{3+}, Nd^{3+}, Sm^{3+}, Eu^{3+}) have been prepared by dissolution in nitric acid *of La_2O_3 (Alfa Aesar, REO (99.99%), Nd_2O_3* (Alfa Aesar, REO), Sm_2O_3 (Alfa Aesar, 99.9% metal basis) and Eu_2O_3 (Merck, purity >99% metal basis), respectively. Zirconyl-oxynitrate solution has been prepared by dissolution of $ZrO(NO_3)_2 \cdot nH_2O$ (Fluka, 99.99% trace metal basis) in distilled water and its concentration has been quantitatively determined by gravimetry. Appropriate volumes of these solutions were mixed and slowly dried. The residue was calcined in alumina crucibles under air at $900\,°C$ ($12\,h$), $1200\,°C$ ($12\,h$), and $1400\,°C$ ($72\,h$) with intermediate grindings. These temperatures are under the pyrochlore to fluorite order-disorder temperature described in the literature[33,62]. These pure lanthanide zirconates with pyrochlore structure were further enriched in ^{17}O as it is the only active nucleus for NMR and possesses a low natural abundance (0.04%)[63]. To do so, the materials were enriched by the gas exchanged (O_2 enriched at 70% mixed with Ar) technique by putting the powders during $24\,h$ at $800\,°C$ in a furnace. These samples were used for analysis by XRD, Raman and ^{17}O MAS NMR in order to avoid the uncertainties led by analysing different samples.

XRD. The patterns of the three [17]O-enriched well crystallized samples (Fig. 1.) were obtained at room temperature on 20 mg of a powdered sample. A Bruker D8 Advance diffractometer (Cu Kα radiation, 40 kV, and 40 mA) with a Bragg−Brentano θ/2θ configuration were used for the analysis. This diffractometer is equipped with a curved Ge monochromator (111) and a Lynxeye linear position-sensitive. The powder patterns were recorded using a step size of 0.0197° across the angular range $10° \leq 2\theta \leq 120°$. Structural analyses were performed by the Rietveld method using Jana2006 software[64]. Peak profile fitting was achieved musing Pseudo-Voigt functions.

^{17}O MAS NMR. The spectra were acquired on a Bruker 9.4 T at the Larmor frequency of 54.25 MHz. To obtain quantitative results for $La_2Zr_2O_7$ and $Sm_2Zr_2O_7$, the spectra were acquired using a one pulse experiment with a very short length of 1 μs[65]. For $Eu_2Zr_2O_7$ and $Nd_2Zr_2O_7$, a Hahn echo was used with pulse durations of 3 μs (π/2) and 6 μs (π) with an echo delay of 16.3 μs (1 rotor period). In addition, two offsets were needed to acquire the full spectrum (to be sure that all the peaks were detected, we performed the experiments with several other offsets but here, we only show at the resonating frequency of the two relevant peaks). Because a Hahn echo experiment was used and the spectra acquired at two offsets, the data are only qualitative. All spectra were externally referenced to [17]O enriched H_2O set at 0 ppm. They were fitted with the DMfit software[66] using the quad first model and the quadrupolar coupling constant, C_Q, and the quadrupolar asymmetry parameter, η_Q, were extracted from the 1D MAS NMR spectra.

Raman spectroscopy. The experiments were performed at room temperature with a Horiba Jobin–Yvon T64000 spectrometer equipped with 1800 gr/mm grating. A 100× objective was used to focus the incident laser operating at 647 nm and collect the backscattered light. Extreme care was taken to avoid sample damage or laser induced heating. Measurements were performed at ~1 mW incident power. No significant change in the spectra was observed in this power range. It must be pointed out that as the samples are enriched in [17]O, the isotopic shifts for all bands is about −1 to −2% which is in very good agreement with the calculated shift for one-phonon excitation and partial substitution (20 to 30% [17]O enrichment) according to the harmonic model:

$$\frac{\triangle\omega_i}{\omega_i} = 1 - \left(\frac{m16_O}{(1-x)m16_O + m17_O}\right)^{1/2}$$ where ω_i is the phonon frequency.

Data availability statement. The datasets generated and/or analyzed during the current study are available from the corresponding author on reasonable request.

References

1. Lumpkin, G. R. Alpha-decay damage and aqueous durability of actinide host phases in natural systems. *J. Nucl. Mater.* **289**, 136–166 (2001).
2. Ewing, R. C., Weber, W. J. & Clinard, F. W. Jr. Radiation effects in nuclear waste forms for high-level radioactive waste. *Prog. Nucl. Energy* **29**, 63 (1995).
3. Nästren, C., Jardin, R., Somers, J., Walter, M. & Brendebach, B. Actinide incorporation in a zirconia based pyrochlore (Nd₁.₈An₀.₂)Zr₂O₇₊ₓ (An=Th, U, Np, Pu, Am). *J. Solid State Chem.* **182**, 1–7 (2009).
4. Ewing, R. C., Weber, W. J. & Lian, J. Nuclear waste disposal—pyrochlore A₂B₂O₇: Nuclear waste form for the immobilization of plutonium and "minor" actinides. *J. Appl. Phys.* **95**, 5949–5971 (2004).
5. Weber, W. J. *et al.* Radiation effects in crystalline ceramics for the immobilization of high-level nuclear waste and plutonium. *J. Mater. Res.* **13**, 1434 (1998).
6. Sattonnay, G., Thomé, L., Monnet, I., Grygiel, C. & Legros, C. Effects of electronic energy loss on the behavior of Nd₂Zr₂O₇ pyrochlore irradiated with swift heavy ions. *Nucl. Instrum. Methods Phys. Res. B* **286**, 254–257 (2012).
7. Perriot, R., Dholabhai, P. P. & Uberuaga, B. P. *Phys. Chem. Chem. Phys.* **18**, 22852–22863 (2016).
8. Park, J. *et al.* Single crystalline pyrochlore nanoparticles with metallic conduction as efficient bi-functional oxygen electrocatalysts for Zn–air batteries. *Energy Environ. Sci.* **10**, 129–136 (2017).
9. Oh, S. H., Black, R., Pomerantseva, E., Lee, J.-H. & Nazar, L. F. Synthesis of a metallic mesoporous pyrochlore as a catalyst for lithium-O2 batteries. *Nature Chem.* **4**, 1004–1010 (2012).
10. Gupta, S. K., Reghukumar, C., Keskar, M. & Kadam, R. M. Revealing the oxidation number and local coordination of uranium in Nd₂Zr₂O₇ pyrochlore: A photoluminescence study. *J. Lumin.* **177**, 166–171 (2016).
11. Liao, J. *et al.* Microwave hydrothermal method and photoluminescence properties of Gd₂Sn₂O₇: Eu³⁺ reddish orange phosphors. *J. Lumin.* **183**, 377–382 (2017).
12. Feng, T., Clarke, D. R., Jiang, D., Xia, J. & Shi, J. Neodymium zirconate (Nd₂Zr₂O₇) transparent ceramics as a solid state laser material. *Appl. Phys. Lett.* **98**, 151105 (2011).
13. Boaro, M. *et al.* Effect of redox treatments on Ce₀.₅₀Zr₀.₅₀O₂ based solid oxide fuel cell anodes. *J. Power Sources* **270**, 79–91 (2014).
14. Zakharchuk, K., Kravchenko, E., Fagg, D. P., Frade, J. R. & Yaremchenko, A. A. Mixed ionic-electronic conductivity and thermochemical expansion of Ca and Mo co-substituted pyrochlore-type Gd₂Ti₂O₇. *RSC Advances* **6**, 70186–70196 (2016).
15. Xu, J. *et al.* Investigation of the magnetic structure and crystal field states of pyrochlore antiferromagnet Nd₂Zr₂O₇. *Phys. Rev. B* **92**, 224430 (2015).
16. Gardner, J. S., Gingras, M. J. P. & Greedan, J. E. Magnetic pyrochlore oxides. *Rev. Mod. Phys.* **82**, 53 (2010).
17. Petit, S. *et al.* Observation of magnetic fragmentation in spin ice. *Nat. Physics* **12**, 746–750 (2016).
18. Guruciaga, C. *et al.* Field-tuned order by disorder in frustrated ising magnets with antiferromagnetic interactions. *Phys. Rev. Lett.* **117**, 167203 (2016).
19. Sickafus, K. E. *et al.* Radiation tolerance of complex oxides. *Science* **289**, 748–751 (2000).
20. Xiao, H. Y., Weber, W. J., Zhang, Y. & Zu, X. T. Ab initio molecular dynamics simulations of ion–solid interactions in zirconate pyrochlores. *Acta Mat.* **87**, 273–282 (2015).
21. Uberuaga, B. P. Complex oxides: Intricate disorder. *Nat. Mater.* **15**, 496–497 (2016).
22. Sickafus, K. E. *et al.* Radiation-induced amorphization resistance and radiation tolerance in structurally related oxides. *Nat. Mater.* **6**, 217–223 (2007).
23. Lumpkin, G. R. *et al.* Ion Irradiation of Ternary Pyrochlore Oxides. *Chem. Mater.* **21**, 2746–2754 (2009).
24. Payne, J. L., Tucker, M. G. & Radosavljević, I. Evans, From fluorite to pyrochlore: Characterisation of local and average structure of neodymium zirconate, Nd₂Zr₂O₇. *J. Solid State Chem.* **205**, 29–34 (2013).
25. Ph D thesis J L Payne, Synthesis, structure and properties of mixed metal oxides: from pyrochlores to fluorites, Durham University, (2010).

26. Shlyakhtinaa, A. V. *et al*. Oxygen interstitial and vacancy conduction in symmetric $Ln_{2\pm x}Zr_{2\pm x}O_{7\pm x/2}$ (Ln=Nd, Sm) solid solutions. *Inorg. Mater.* **50**, 1035–1049 (2014).

27. Shamblin, J. *et al*. Probing disorder in isometric pyrochlore and related complex oxides. *Nat. Mater.* **15**, 507–511 (2016).

28. Zhang, F. X., Lang, M., Liu, Z. & Ewing, R. C. Pressure-induced disordering and anomalous lattice expansion in $La_2Zr_2O_7$ pyrochlore. *Phys. Rev. Lett.* **105**, 015503 (2010).

29. Subramanian, M. A., Aravamudan, G. & Rao, G. V. S. Oxide pyrochlores - A review. *Prog. Solid State Chem.* **15**, 55–143 (1983).

30. Minervini, L., Grimes, R. W. & Sickafus, K. E. Disorder in pyrochlore oxides. *J. Am. Ceram. Soc.* **83**, 1873–78 (2000).

31. Scheetz, B. E. & White, W. B. Characterization of anion disorder in zirconate $A_2B_2O_7$ compounds by Raman spectroscopy. *J. Am. Ceram. Soc.* **62**, 468–470 (1979).

32. Sanjuan, M. L. *et al*. Raman and X-ray absorption spectroscopy study of the phase evolution induced by mechanical milling and thermal treatments in $R_2Ti_2O_7$ pyrochlores. *Phys. Rev. B* **84**, 104207 (2011).

33. Jiang, C., Stanek, C. R., Sickafus, K. E. & Uberuaga, B. P. First-principles prediction of disordering tendencies in pyrochlore oxides. *Phys. Rev. B* **79**, 104203 (2009).

34. Finkeldei, S. *et al*. Composition dependent order-disorder transition in $Nd_xZr_{1-x}O_{2-0.5x}$ pyrochlores: A combined structural, calorimetric and ab initio modeling study. *Acta Mat.* **125**, 166–176 (2017).

35. Blanchard, P. E. R. *et al*. Does Local Disorder Occur in the Pyrochlore Zirconates? *Inorg. Chem.* **51**, 13237–13244 (2012).

36. Van Dijk, M. P. *et al*. Electrical and catalytic properties of some oxides with the fluorite or pyrochlore structure. *Mat. Res. Bull.* **19**, 1149–1156 (1984).

37. Ciomaga Hatnean, M. *et al*. Structural and magnetic investigations of single-crystalline neodymium zirconate pyrochlore $Nd_2Zr_2O_7$. *Phys. Rev. B* **91**, 174416 (2015).

38. Kong, L. *et al*. A novel chemical route to prepare $La_2Zr_2O_7$ pyrochlore. *J. Am. Ceram. Soc.* **96**, 935–941 (2013).

39. Ciomaga Hatnean, M., Lees, M. R. & Balakrishnan, G. Growth of single-crystals of rare-earth zirconate pyrochlores, $Ln_2Zr_2O_7$ (with Ln=La, Nd, Sm, and Gd) by the floating zone technique. *J. Crys. Growth* **418**, 1–6 (2015).

40. Klobes, B., Finkeldei, S., Röhrig, W., Bosbach, D. & Hermann, R. P. Hyperfine interactions in and lattice parameters of pyrochlore and defect fluorite $(Eu_{1-x}Nd_x)_2Zr_2O_7$. *J. Phys. Chem. Solids* **79**, 43–48 (2015).

41. Solomon, S., George, A., Thomas, J. K. & John, A. Preparation, characterization, and ionic transport properties of nanoscale $Ln_2Zr_2O_7$ (Ln=Ce, Pr, Nd, Sm, Gd, Dy, Er, and Yb) Energy Materials. *J. Elec. Mater.* **44**, 28–37 (2015).

42. Singh, S. *et al*. Manifestation of geometric frustration on magnetic and thermodynamic properties of the pyrochlores $Sm_2X_2O_7$ (X=Ti, Zr). *Phys. Rev. B* **77**, 054408 (2008).

43. Qu, Z., Wan, C. & Pan, W. Thermal Expansion and Defect Chemistry of MgO-Doped $Sm_2Zr_2O_7$. *Chem. Mater.* **19**, 4913–4918 (2007).

44. Anithakumari, P., Grover, V., Nandi, C., Bhattacharyya, K. & Tyagia, A. K. Utilizing non-stoichiometry in $Nd_2Zr_2O_7$ pyrochlore: exploring superior ionic conductors. *RSC Adv.* **6**, 97566–97579 (2016).

45. Kim, N. & Grey, C. P. ^{17}O MAS NMR study of the oxygen local environments in the anionic conductors $Y_2(B_{1-x}B'_x)_2O_7$ (B; B'=Sn; Ti, Zr). *J. Solid State Chem.* **175**, 110–115 (2003).

46. Palumbo, J. L., Schaedler, T. A., Peng, L., Levi, C. G. & Grey, C. P. ^{17}O NMR studies of local structure and phase evolution for materials in the $Y_2Ti_2O_7$–$ZrTiO_4$ binary system. *J. Solid State Chem.* **180**, 2175–2185 (2007).

47. Seymour, I. D. *et al*. Characterizing oxygen local environments in paramagnetic battery materials via ^{17}O NMR and DFT Calculations. *J. Am. Chem. Soc.* **138**, 9405–9408 (2016).

48. Verkhovskii, S. *et al*. ^{17}O NMR evidence for vanishing of magnetic polarons in the paramagnetic phase of ceramic $CaMnO_3$. *Phys. Rev. B* **81**, 144415 (2010).

49. Kong, X. *et al*. Solid-state ^{17}O NMR spectroscopy of paramagnetic coordination compounds. *Angew. Chem., Int. Ed.* **54**, 4753 (2015).

50. Martel, L. *et al*. Structural investigation of uranium−neptunium mixed oxides using XRD, XANES, and ^{17}O MAS NMR. *J. Phys. Chem. C* **118**, 27640–27647 (2014).

51. Grey, C. P., Dobson, C. M., Cheetham, A. K. & Jakeman, R. J. B. Studies of rare-earth stannates by tin-119 MAS NMR. The use of paramagnetic shift probes in the solid state. *J. Am. Chem. Soc.* **111**, 505–511 (1989).

52. Yang, S., Shore, J. & Oldfield, E. Oxygen-17 Nuclear magnetic resonance spectroscopic study of the lanthanide oxides. *J. Magn. Reson.* **99**, 408–412 (1992).

53. Bregiroux, D., Audubert, F., Charpentier, T., Sakellariou, D. & Bernache-Assollant, D. Solid-state synthesis of monazite-type compounds $LnPO_4$ (Ln=La to Gd). *Solid State Sciences* **9**, 432–439 (2007).

54. Ashbrook, S. E. *et al*. New insights into phase distribution, phase composition and disorder in $Y_2(Zr,Sn)_2O_7$ ceramics from NMR spectroscopy. *Phys. Chem. Chem. Phys.* **17**, 9049–9059 (2015).

55. Tucker, M. C. *et al*. ^7Li and ^{31}P magic angle spinning nuclear magnetic resonance of $LiFePO_4$-type materials. *Electrochem. Solid-State Lett.* **5**, A95–A98 (2002).

56. Michel, D., Perez y Jorba, M. & Collongues, R. Study by Raman spectroscopy of order-disorder phenomena occurring in some binary oxides with fluorite-related structures. *J. Raman Spectrosc.* **5**, 163–180 (1976).

57. Sayed, F. N. *et al*. $Sm_{2-x}Dy_xZr_2O_7$ pyrochlores: probing order-disorder dynamics and multifunctionality. *Inorg. Chem.* **50**, 2354–2365 (2011).

58. Kroumova, E., *et al*. H., Bilbao Crystallographic Server: Useful databases and tools for phase-transition studies phase transitions **76**, 155–170 (2003).

59. Kosacki, I., Suzuki, T., Anderson, H. U. & Colomban, P. Raman scattering and lattice defects in nanocrystalline CeO_2 thin films. *Solid State Ionics* **149**, 99–105 (2002).

60. Arenas, D. J. *et al*. Raman study of phonon modes in bismuth pyrochlores. *Phys. Rev. B* **82**, 214302 (2010).

61. Fischer, M., Malcherek, T. & Bismayer, U. Structure and stability of $Cd_2Nb_2O_7$ and $Cd_2Ta_2O_7$ explored by ab initio calculations. *Phys. Rev. B* **78**, 014108 (2008).

62. Rushton, M. J. D., Grimes, R. W., Stanek, C. R. & Owens, S. Predicted pyrochlore to fluorite disorder temperature for $A_2Zr_2O_7$ compositions. *J. Mater. Res.* **19**, 1603–1604 (2004).

63. Ashbrook, S. E. & Smith, M. E. Solid state ^{17}O NMR—an introduction to the background principles and applications to inorganic materials. *Chem. Soc. Rev.* **35**, 718–735 (2006).

64. Petricek, V., Dusek, M., Palatinus, L., Jana 2006: The Crystallographic Computing System; Institute of Physics: Czech Republic (2006).

65. Massiot, D., Bessada, C., Coutures, J. P. & Taulelle, F. A quantitative study of ^{27}Al MAS NMR in crystalline YAG. *J. Magn. Reson.* **90**, 231–242 (1990).

66. Massiot, D. *et al*. Modelling one and two-dimensional solid-state NMR spectra. *Magn. Reson. Chem.* **40**, 70–76 (2002).

Acknowledgements

Author Contributions

The samples were synthesized by K.P.; the XRD, MAS-NMR and Raman experiments were respectively acquired by J.-F. V., L. M. and M. N.; J.S. contributed to the version used here. All the authors contributed to the discussion of the results and the preparation of the manuscript.

Additional Information

Supplementary information accompanies this paper at https://doi.org/10.1038/s41598-017-12544-8.

Competing Interests: The authors declare that they have no competing interests.

Publisher's note: Springer Nature remains neutral with regard to jurisdictional claims in published maps and institutional affiliations.